Supplementary

Stanley Cheung*, Di Liang*, Yuan Yuan*, Yiwei Peng, Yingtao Hu, Geza Kurczveil, and Raymond G. Beausoleil

Hewlett Packard Enterprise, Large-Scale Integrated Photonics Lab, Milpitas, CA. 95035, USA
*stanley.cheung@hpe.com, di.liang@ieee.org, yuan.yuan@hpe.com

Supplementary Note 1:

Electro-optical simulations and design

A 2-D electrical solver (SILVACO ATLAS [7]) was used to study the non-volatile electrical behavior of the III-V/Si CTM structure. This modeling software has been used successfully in other theoretical optical non-volatile structures[8,9]. The program numerically solves the Poisson, charge continuity equations, drift-diffusion transport, and quantum tunneling mechanisms. The models involved include Fermi-Dirac statistics, Shockley-Read-Hall recombination, quantum tunneling that includes direct and Fowler-Nordheim [7]. The semiconductor material parameters used for optical and electronic TCAD simulations are listed in Table *1*: Material parameters used in electro-optical simulations.

Table 1: Material parameters used in electro-optical simulations

Material	E_g (eV)	χ (eV)	VBO (eV)	CBO (eV)	n	N_{TC} (cm^{-3})	φ_d (eV)
Al_2O_3	7.0 [10]	1.5 [11–13]	3.2 [10]	2.7 [10]	1.75	-	-
HfO_2	5.7 [10]	2.5 [10]	2.7 [10]	1.9 [10]	1.9	10^{19} - 10^{20} [9,14,15]	2.0 [16–19]
SiO_2	8.9 [10]	1.3 [10]	4.5 [10]	3.3 [10]	1.44	-	-
Si	1.1 [10]	4.1 [10]	-	-	3.507 [20]	-	-
GaAs	1.43 [7]	4.07 [7]	-	-	3.406 [20]	-	-

E_g: Energy gap, χ: electron affinity, n: refractive index (at λ = 1310 nm), VBO: valance band offset, CBO: conduction band offset, N_{TC}: trap density, φ_d: electron trap level

Once the structure is built with the appropriately assigned models and trapped charge density, the band diagrams, C-V curves, and electron/hole concentrations are simulated for various biases. The spatial profiles of the change in electron/hole concentrations ($\Delta P(x,y)$ and $\Delta N(x,y)$) are then exported and used to calculate a spatial refractive index change $\Delta n(x,y)$ by the following equation [21,22]:

$$\Delta n(x,y) = -6.2\times10^{-22}\,\Delta N(x,y) - 6.0\times10^{-18}\,\Delta P(x,y) \qquad (1)$$

This equation is valid for a wavelength λ = 1310 nm and is used throughout the manuscript. Next, this spatial refractive index change $\Delta n(x,y)$ is exported into a 2D-FDE optical mode solver (Lumerical) and the non-volatile change in effective index ($\Delta_{neff,non\text{-}volatile}$) is calculated. This change can then be used to calculate non-volatile phase shifts on photonic devices such as ring resonators, Mach-Zehnder interferometers, filters, etc. The figure below illustrates the simulation procedure:

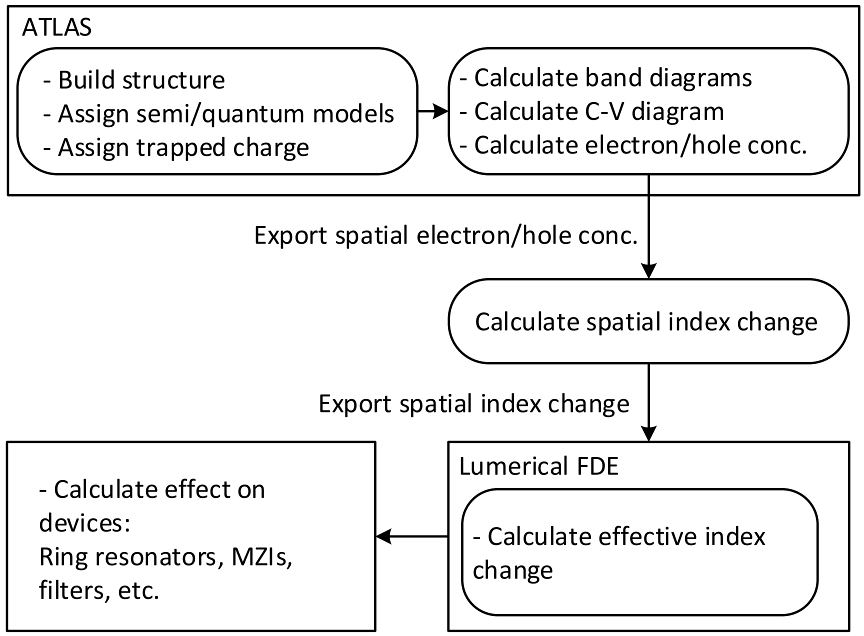

Fig. 1. Flowchart of electro-optical simulation procedure for III-V/Si CTM structure

III-V/Si CTM MZI designs

An example design and mask layout of the III-V/Si CTM MZI is shown in Fig. *2*b-c. The III-V/Si CTM cell is located on the upper arm with a length of $L_{1,iii-v/si} = 325$ µm. Taking into account the different effective indices and lengths between the upper and lower arms, the total optical path length difference is ~ 5.206 µm. The p-doping is defined 2 µm away from the edge of the silicon waveguide and test structures indicated little to no effect on optical losses. The n-GaAs has a 200 nm overhang to the edge of the silicon waveguide such that III-V/Si bonding remains intact while avoiding contact with silicon pillars. A fully etched deep trench is defined in between the MZI arms such that the p-Si is electrically isolated from the wafer-bonded n-GaAs region.

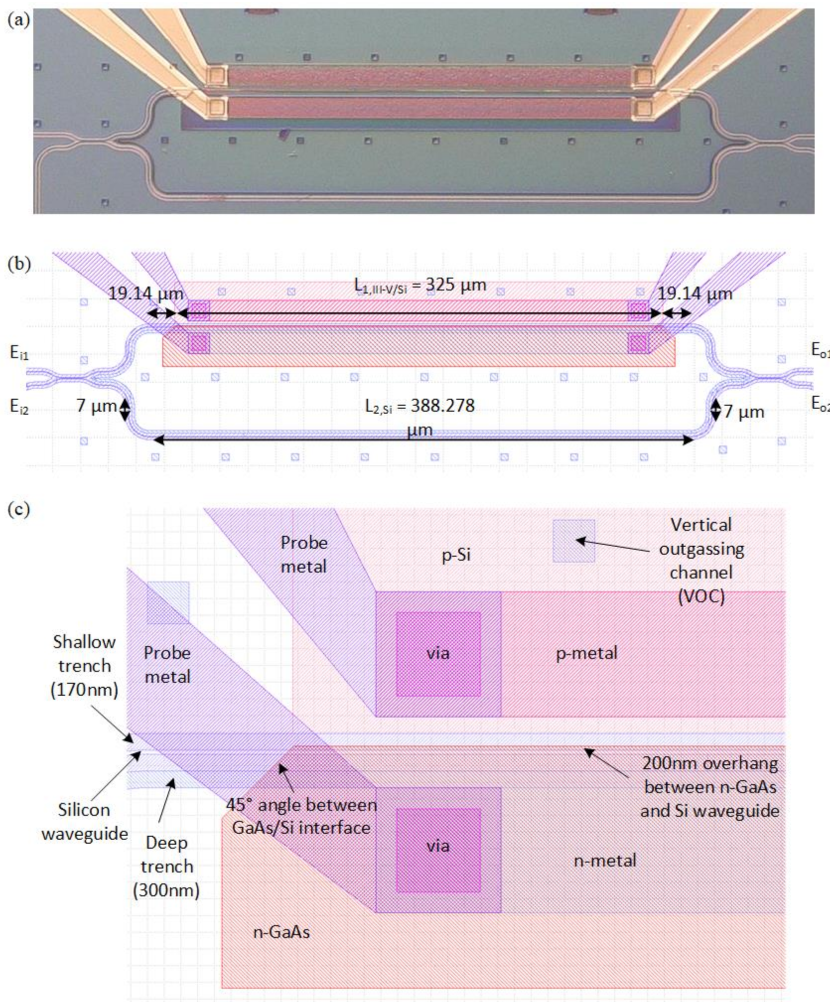

Fig. 2. (a) Microscope image of fabricated III-V/Si CTM MZI, (b) mask layout, design, and dimensions, (c) layer identification and III-V/Si interface details

The electric field transmission function of the top/bottom arm of the MZI (E_{o1}, E_{o2}) can be modeled with the following transfer matrix:

$$\begin{bmatrix} E_{o1} \\ E_{o2} \end{bmatrix} = \begin{bmatrix} t & jr \\ jr & t \end{bmatrix} \begin{bmatrix} e^{i\phi_1 - \zeta_1} & 0 \\ 0 & e^{i\phi_2 - \zeta_2} \end{bmatrix} \begin{bmatrix} t & jr \\ jr & t \end{bmatrix} \begin{bmatrix} E_{i1} \\ X_{i2} \end{bmatrix} \tag{9}$$

$$I_{o1} = |E_{o1}|^2 \, , \, I_{o2} = |E_{o2}|^2 \tag{10}$$

$$\begin{gathered} \phi_1 = \beta_{1,si} L_{1,si} + \beta_{1,iii-v/si} L_{1,iii-v/si} \\ \phi_1 = \beta_{2,si} L_{2,si} \\ \zeta_1 = \frac{1}{2}\alpha_{1,si} L_{1,si} - \frac{1}{2}\alpha_{1,iii-v/si} L_{1,iii-v} \\ \zeta_2 = \frac{1}{2}\alpha_{2,si} L_{2,si} \end{gathered} \tag{11}$$

$\beta_{1,si}$, $\beta_{2,si}$, $\beta_{1,iii\text{-}v/si}$, represent the propagation constants of the top arm silicon, bottom arm silicon, and top arm III-V/Si CTM waveguide respectively. $\alpha_{1,si}$, $\alpha_{2,si}$, $\alpha_{1,iii\text{-}v/si}$ represent the optical losses in the top arm, bottom arm, and top arm III-V CTM waveguide respectively. $L_{1,si}$, $L_{2,si}$, $L_{1,iii\text{-}v/si}$ represent the corresponding lengths. Using the equations defined above, the calculated transmission spectrum is shown in Fig. *3*a. This particular MZI configuration yields a free-spectral-range (FSR) of ~ 25.6 nm. A trapped charge concentration of $Q_{TC} = 9 \times 10^{19}$ cm^{-3} is enough to shift the spectrum by 1.567 nm (0.38π phase shift) for a CTM length of 325 μm. Larger phase shifts would entail either longer phase shifts or increasing charge trap defects in the CTM structure.

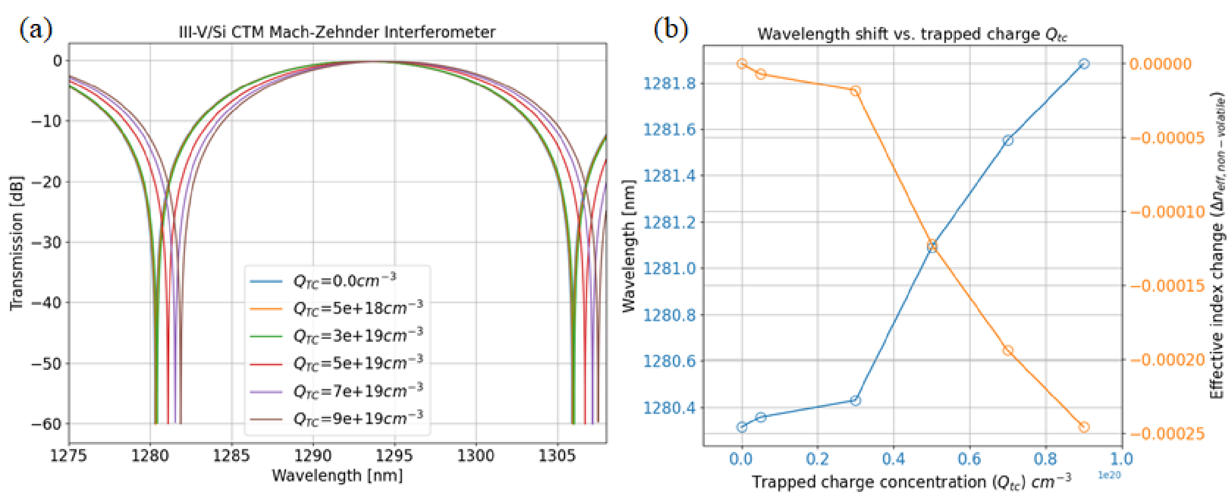

Fig. 3 III-V/Si CTM MZI (a) transmission spectrum from port E01, (b) absolute wavelength and corresponding shift for various values of trapped charge concentration.

III-V/Si CTM cascaded ring resonator filter designs

High order cascaded ring resonators often find utility as compact, flat-top filters with low channel crosstalk. In this section we explore the design of 2nd order cascaded rings and the non-volatile filter shapes as a result of integrating III-V/Si CTM memory cells as shown in Fig. 4a-b. In our particular design, we cascade two 2nd order ring resonators onto the same bus waveguide to realize a 2 channel (de-) interleaver. The (de-) interleaver channels are typically measured from ports Out1b and Out2b. However, for the rest of this section, we focus on ports Out3 since the effect on the two resonances are more clear and pronounced. The power coupling coefficients between the rings are chosen such that $\kappa_1^2 = 0.25k\kappa_0^4$ results in a maximally flat filter condition for ports Out1b, Out2b, if k = 2 and $\kappa_0^2 = 0.35$ [25,26]. Each cascade double ring structure can be divided into "Ring bank 1" and "Ring bank 2", with the first ring bank designed for 130 GHz spacing. The electric field transmission function of the cascaded ring resonator filter can be modeled with the following transfer matrix [25,26]:

$$\begin{bmatrix} E_{out2b} \\ E_{out2a} \end{bmatrix} = (PQ)^N P \begin{bmatrix} E_{in} \\ 0 \end{bmatrix} = \begin{bmatrix} T_{00} & T_{01} \\ T_{10} & T_{11} \end{bmatrix} \tag{4}$$

$$P = \begin{bmatrix} -\dfrac{t}{j\kappa} & \dfrac{1}{j\kappa}e^{-j\beta L_c} \\ -\dfrac{t^2+\kappa^2}{j\kappa}e^{j\beta L_c} & \dfrac{t}{j\kappa} \end{bmatrix}, \quad Q = \begin{bmatrix} 0 & ae^{j\beta L_r} \\ \dfrac{1}{a}e^{-j\beta L_r} & 0 \end{bmatrix} \tag{5}$$

$$a = 10^{-AL_r 100/20}, \; L_r = 0.5L_c \tag{7}$$

$$I_{out3} = \left|\frac{T_{00}}{T_{01}}\right|^2, \; I_{out2b} = \left|T_{10} - \frac{T_{00}T_{11}}{T_{01}}\right|^2 \tag{8}$$

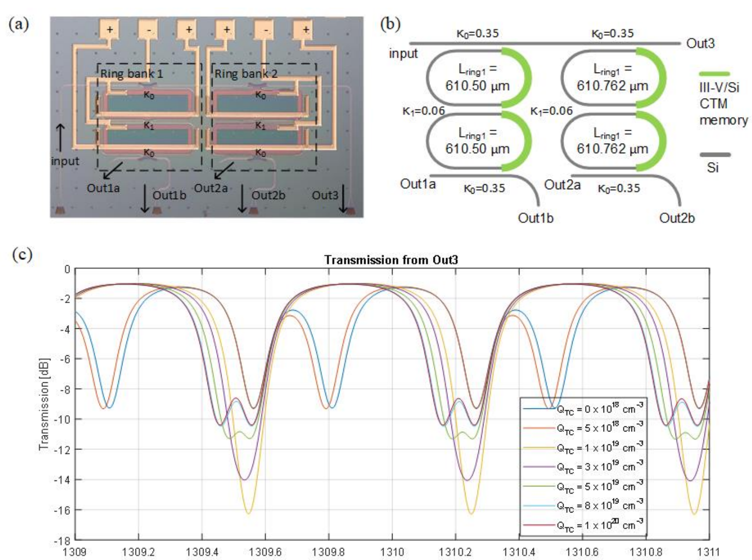

Fig. 4 (a) Microscope image of fabricated 2 channel (de-)interleaver based on cascaded 2nd order ring resonator filters, (b) schematic indicating lengths, coupling coefficients and port identification, (c) calculated changes in spectrum based on charge trap densities.

The field transfer coefficients, propagation constant, ring circumference, and ring order are defined as t, κ, β, L_c, and N. If we only bias the ring resonators in "Ring bank 2", and use the same effective index changes due to trapped charges as the previous devices, we can see the effect on the 2nd order ring resonator filter shape at port Out3 as shown in Fig. *4*c. The resonance belonging to "Ring bank 1" (port Out1b) remains larger unchanged, whereas the resonance belonging to "Ring bank 2" shifts dramatically, thus altering the filter shape.

Post-fabrication phase error correction

An alternative use of the non-volatile III-V/Si CTM cell is the role it can play in post-fabrication trimming or permanent phase error correction without consuming static electrical power. Inherent to the high index contrast of the silicon photonic material system, phase sensitive devices such as arrayed waveguide gratings (AWGs), lattice filters, and (de-)interleavers are sensitive to phase errors and are dependent on waveguide width, thickness, and refractive index non-homogeneity. In this case, the ability to use non-volatile phase tuning to correct the aforementioned errors is essential to minimizing power consumption. Changes in resonant the resonant wavelength can be described by the following equation [4]:

$$\Delta\lambda_0 = \left(\lambda_0 / n_g\right)\sqrt{\left(dn_{eff} / dw \cdot \Delta w\right)^2 + \left(dn_{eff} / dt \cdot \Delta t\right)^2} \qquad (12)$$

$\lambda_0, n_{eff}, n_g, \Delta w,$ and Δt are the free-space wavelength, effective index, group index, width variation, and thickness variation respectively. Along with the group index $n_g = n_{eff} - \lambda_0 \cdot dn_{eff} / d\lambda$, the resonant wavelength variation for each dimension can be calculated as: $\Delta\lambda_0 / \Delta w = (\lambda_0 / n_g)(dn_{eff} / dw)$ and $\Delta\lambda_0 / \Delta t = (\lambda_0 / n_g)(dn_{eff} / dt)$. The effective index and group index as a function of width and thickness are plotted in Fig. 5a – b. It can be seen that both values increase as waveguide dimensions increase because of increased modal confinement. Fig. 5c – d illustrates width sensitivity (dn_{eff}/dw) and thickness sensitivity (dn_{eff}/dt). Throughout the paper, single-mode III-V/Si CTM waveguides are used and have design dimensions of height = 300 nm, width = 500nm, etch depth = 170nm, and GaAs thickness of 150 nm, thus resulting in effective index variations of $dn_{eff}/dw = 5.80 \times 10^{-4}$ /nm and $dn_{eff}/dt = -4.44 \times 10^{-5}$ /nm. Typically, the most critical parameter in controlling phase errors is the starting SOI wafer thickness uniformity.

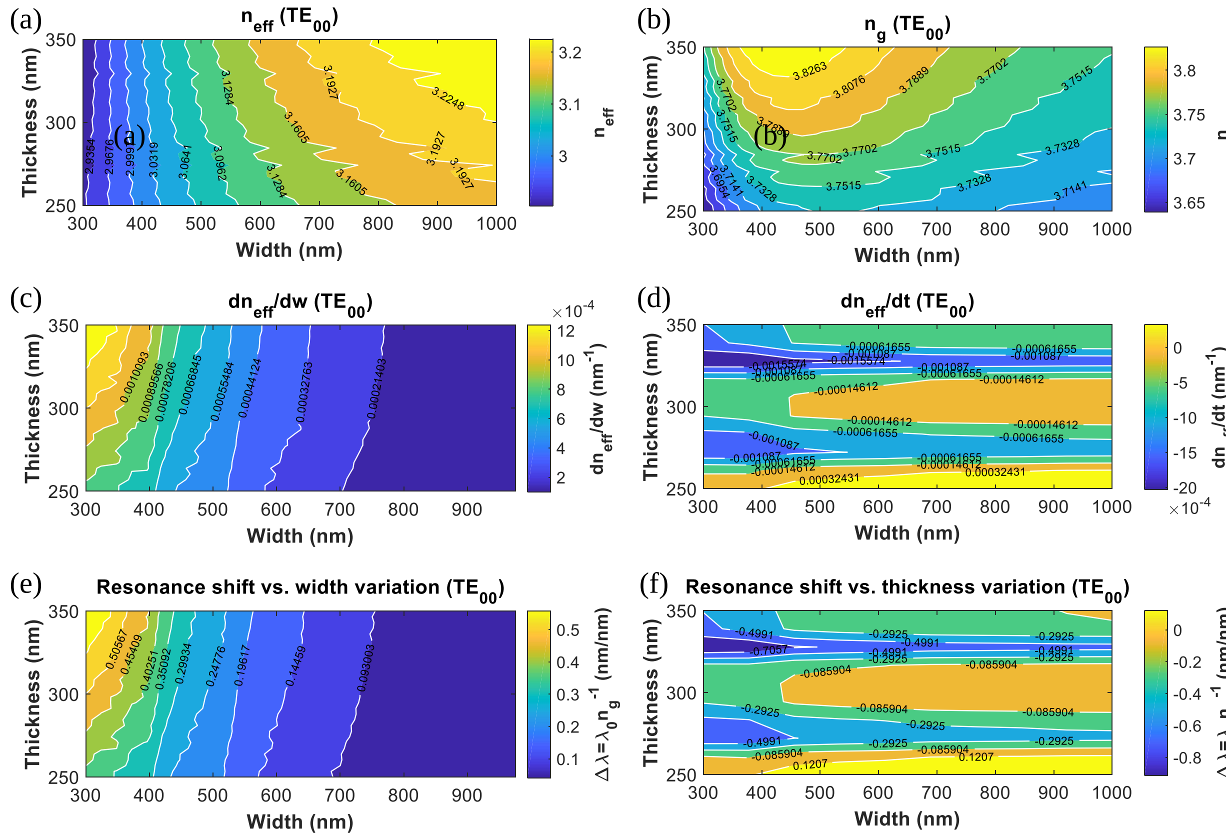

Fig. 5 III-V/Si CTM optical mode calculations for (a) effective index (n_{eff}), (b) group index (n_g), (c) effective index change vs. waveguide width (dn_{eff}/dw), (d) effective index change vs. waveguide thickness (dn_{eff}/dt), (e) wavelength shift ($\Delta\lambda_0/dw$) vs. waveguide width, (f) wavelength shift vs. waveguide thickness ($\Delta\lambda_0/dt$).

However, for the III-V/Si case, the GaAs thickness reduces this SOI thickness sensitivity significantly, and as a result, width variations play a larger role in phase errors by an order of magnitude. The wavelength shift variation are $\Delta\lambda_0/dw = 0.2457$ nm/nm and $\Delta\lambda_0/dt = -0.0187$ nm/nm as shown in Fig. 5e – f. The use of wider waveguides can significantly reduce $\Delta\lambda_0/dw$ by another order of magnitude, however, the TE01 mode starts to appear at a width of 600 nm as seen in Fig. 5b. We believe, the III-V/Si CTM waveguide dimensions used throughout this paper offers the best design trade-off in terms of low dn_{eff}/dw and dn_{eff}/dt while maintaining single-mode operation. However, if we assume a charge trap concentration of $Q_{TC} > 9\times 10^{19}$ cm^{-3} and a $dn_{eff}/dw = 5.80 \times 10^{-4}$ /nm, the III-V/Si CTM cell may be capable of correcting several nm of errors in waveguide width.

Supplementary Note 2: Fabrication

In-house device fabrications starts with a 100 mm SOI wafer which consists of a 350 nm thick top silicon layer and a 2 µm buried oxide (BOX) layer. The top silicon is thinned down to 300 nm by thermal oxidation and buffered hydrofluoric (HF) acid etching, thus leaving a clean silicon surface. Silicon waveguides are defined by a deep-UV (248 nm) lithography stepper and boron is implanted to create p ++ silicon contacts. Grating couplers, silicon rib waveguides, and vertical out-gassing channels (VOCs) are respectively patterned using the same deep-UV stepper and then subsequently etched 170 nm with Cl_2-based gas chemistry. Next, the silicon wafer goes through a Piranha clean followed by buffered hydrofluoric (HF) acid etching to remove any hard masks. Next, an oxygen plasma clean is performed followed by a SC1 and SC2 clean. The III-V wafer goes through a solvent clean consisting of acetone, methanol, and IPA, followed by oxygen plasma cleaning and a NH_4OH:H_2O (1:10) dip for 1 minute. Next a dielectric of Al_2O_3 is deposited onto both GaAs and Si wafers via atomic layer deposition (ALD) by using 5 cycles of trimethylaluminum (TMA) + H_2O with a target thickness of 0.5 nm on each side. All ALD deposition temperatures are performed at 300 °C. Next, a thickness target of 3 nm HfO_2 is deposited on each sample via 30 cycles of tetrakis (ethylmethylamino) hafnium (TEMAH) + H_2O. Finally, a thickness target of 1 nm Al_2O_3 is deposited on each sample via 10 cycles of TMA + H_2O. The two samples are then mated manually at room temperature and then wafer-bonded under pressure for 250 °C (2 hour ramp) for a total of 15 hours. After wafer-bonding, the backside of the III-V is mechanically lapped until ~ 100 µm of III-V is left. An $Al_{0.20}Ga_{0.80}As$ etch stop layer allows selective removal of the remaining GaAs substrate via wet etching (H_2O_2:NH_4OH (30:1)). The $Al_{0.20}Ga_{0.80}As$ is finally removed in buffered hydrofluoric acid (BHF), thus leaving a 150 nm-thick n-GaAs thin film on top of the SOI substrate. A combination of Ge/Au/Ni/Au/Pd/Ti (400/400/240/4000/200/200 Å) is deposited onto the n-GaAs as an n-contact layer. Next, the III-V film is defined and dry etched for device regions that require the use of phase tuning. Metal contact with the p-Si consists of Ni/Ge/Au/Ni/Au/Ti (50/300/300/200/5000/200 Å). Next, a plasma enhanced chemical vapor deposition (PECVD) SiO_2 cladding is deposited and the vias are defined and etched. Finally, Ti/Au metal probe pads are defined to make contact with n-GaAs and p-Si layers. The relevant fabricated devices can be seen in Fig. *7*a-b.

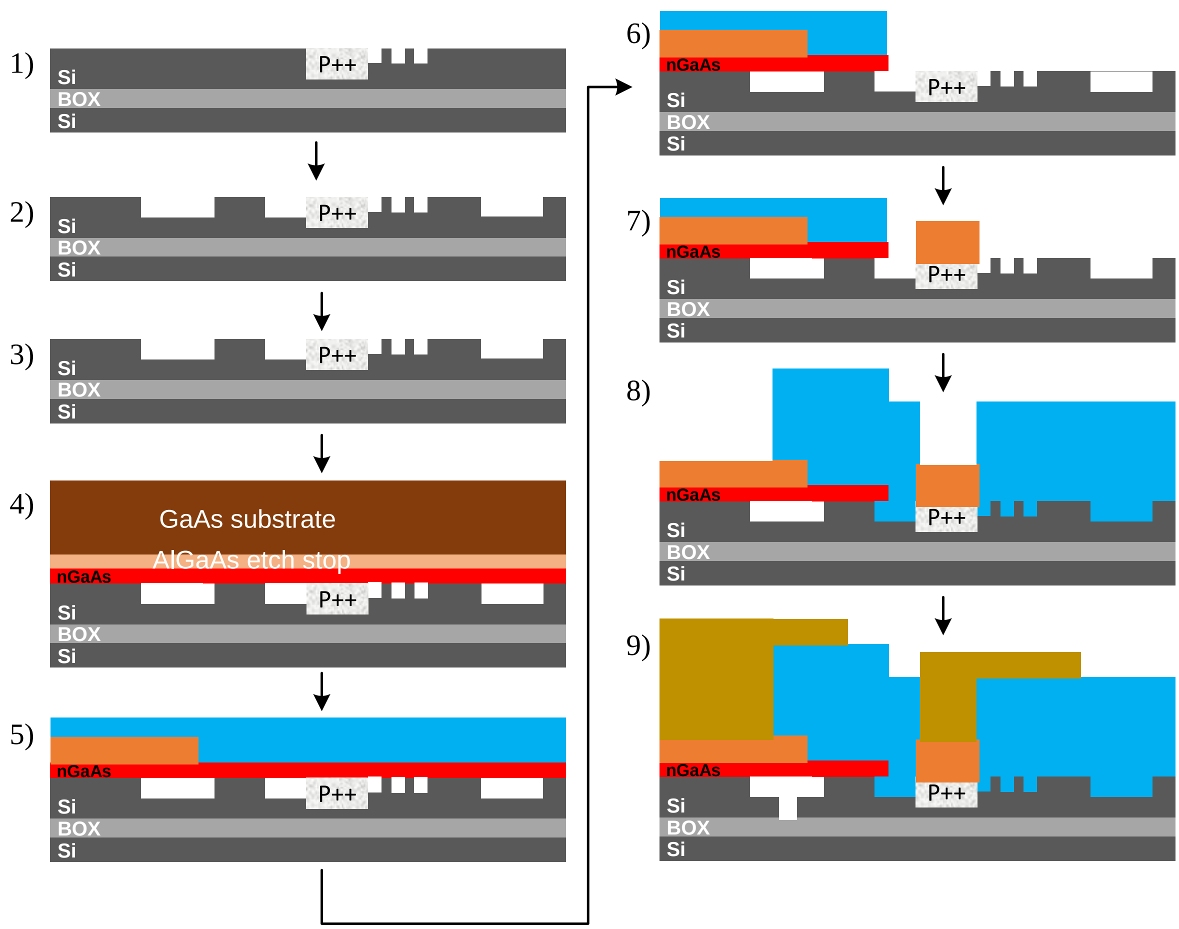

Fig. 6 Fabrication flow of heterogeneous III-V/Si CTM device.

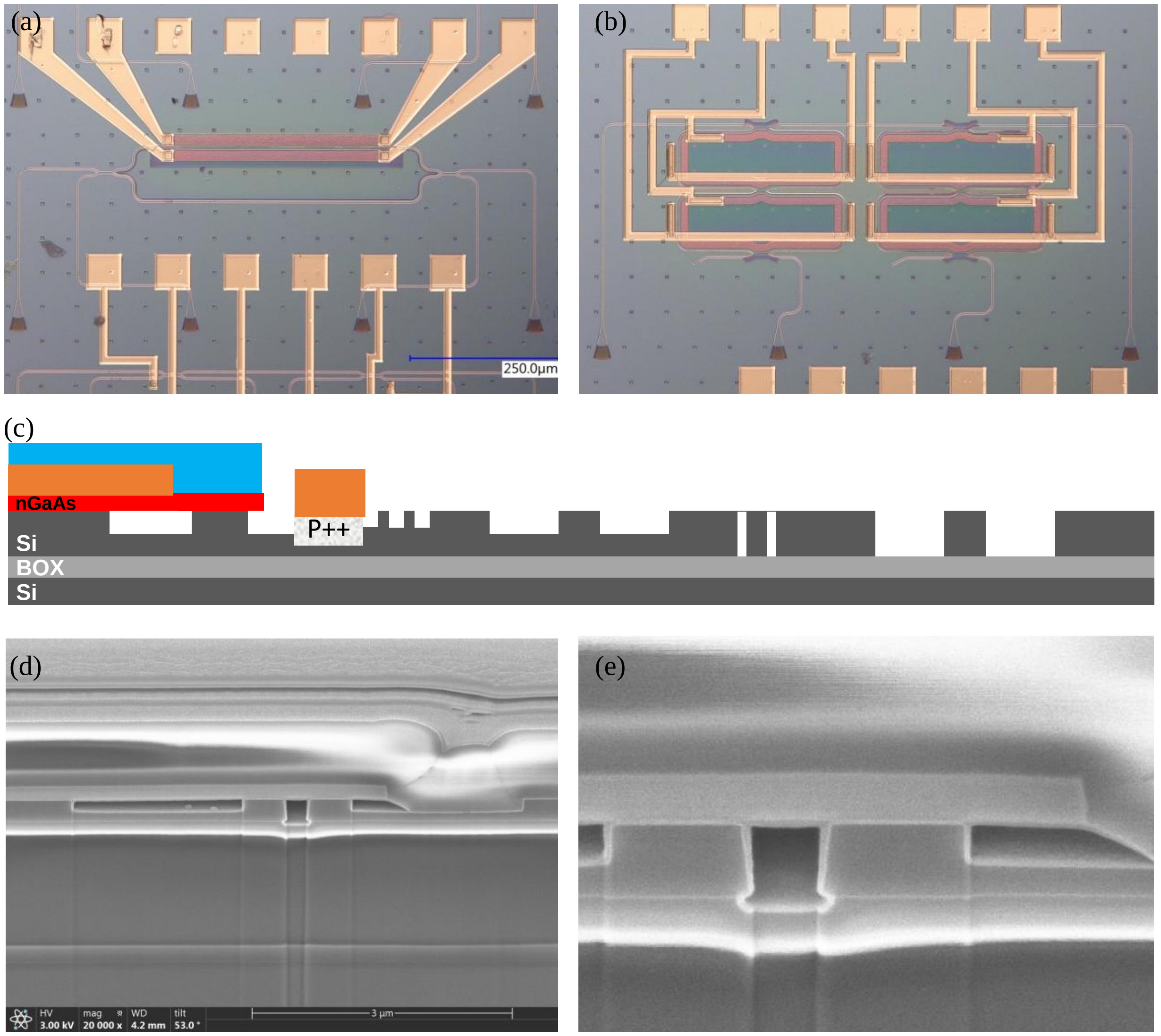

Fig. 7. Microscope images of fabricated III-V/Si CTM (a) MZI, and (b) 2nd order cascaded ring resonators. (c) Schematic of 2-D cross-section. (d) - (e) SEM image of cross-section.

Supplementary Note 3: Measurements

The spectral response of the devices were characterized with a Thorlabs superluminescent diode (SLD) capable of 40 nm bandwidth (1290 – 1330 nm). The 100 mm wafer is vacuum mounted onto a stainless steel chuck on a semi-automatic probe station. Light is vertically coupled in/out of devices via grating couplers with a 7 ° polished fiber array w (250 μm pitch). Polarization control is performed with the use of a polarization controller and maximized for peak transmission on a straight test waveguide. C-V, I-V, and optical spectra measurements are performed with an Agilent E4980A, Keithley 2400, and Yokogawa AQ6370D respectively. The pre-bonded 0.5 μm wide straight waveguide TE losses were determined to be about ~ 9.2 dB/cm for a wavelength of 1310 nm from a series of cutback test structures. 0.8 μm wide straight waveguide TE losses were about 9.8 dB/cm. After III-V removal, TE waveguide losses were measured to be ~ 21.1 and 42.2 dB/cm for the 0.8 and 0.5 μm wide waveguides, respectively. Circular bends of radius = 2, 5, 7, 14 μm had bend losses = 1.22, 0.83, 0.3, 0.08 dB/90° bend respectively. Spline bends with a radius = 4 μm and angle = 45, 10, 5 ° have measured bend losses = 0.23, 0.86, 1.09 dB/bend respectively. The angular coverage of a spline bend is discussed at length in [27]. A spline bend with radius = 2 μm exhibited a bend loss = 0.74 dB/bend. Grating coupler loss before and after bonding were calculated to be 7.7 and 7.8 dB/coupler indicating negligible effect after III-V removal. We numerically analyze the reflection and insertion loss of the III-V/Si interface as a function of angle between the III-V and Si.

(a)

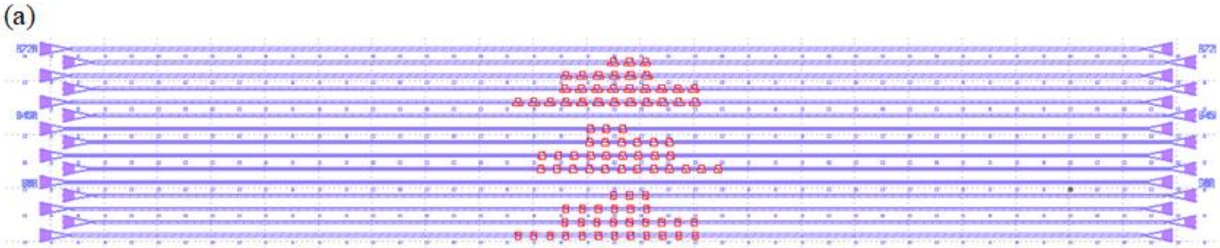

(b)

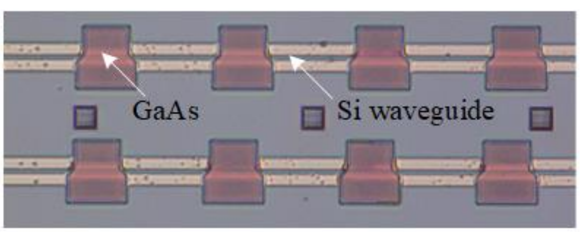

(c)

	0 deg	45 deg	72 deg
Interface losses	1.1 dB	0.7 dB	0.3 dB

(d) (e) (f)

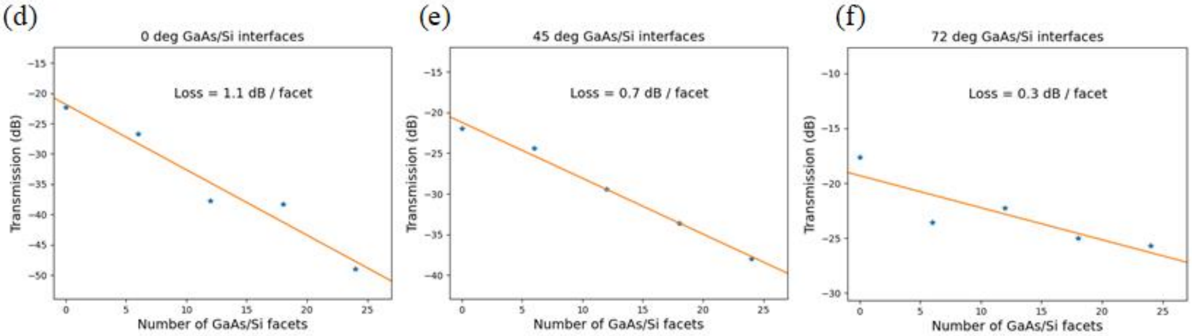

Fig. 8 (a) Mask layout of test structures for extracting III-V/Si angle interface losses, (b) image of fabricated III-V/Si interface, (c) summary of measured losses for θ = 0, 45, 72 °, and (d) transmission measurements used to extract single interface losses for respective θ.

3-dimensional finite-difference-time-domain (3D-FDTD) simulations show minimal reflection (< - 60 dB) back into the fundamental TE_{00} mode at an angle of 45 ° with an insertion loss of 0.36 dB/facet. Minimal insertion loss was found to occur at 72 °, but with increased reflection into the main TE_{00} mode. Throughout this paper, an angle of $\theta = 45$ ° is used for all fabricated and measured devices. Angled GaAs/Si interface losses were evaluated by cutback loss structures as illustrated in Fig. *8*a. The cutback test structures are divided into 3 groups that represent an angle of $\theta_{III\text{-}V/Si} = 0, 45, 72$ °. The interface losses for angles of 0 °, 45 °, and 72 ° were measured to be 1.08, 0.69, and 0.29 dB/facet respectively and match up with simulated values quite well. *Fig. 9*a shows the measured transmission spectra of the CTM MZI for initial and non-volatile states as described in *Fig. 2*. By applying a write operation, a $\Delta\lambda_{non\text{-}volatile} = 1.16$ nm is achieved which corresponds to a $\Delta n_{eff,\ non\text{-}volatile} = 2.5 \times 10^{-4}$. From transfer matrix modeling, the directional couplers were found to have a power transfer ratio of ~ 30 % instead of the ideal case of 50 %. This is responsible for the low ER, however, 50 % power couplers can yield ER > 50 dB assuming a loss of 3 dB/cm. A new fabrication run is currently underway with improved directional couplers for the CTM MZIs.

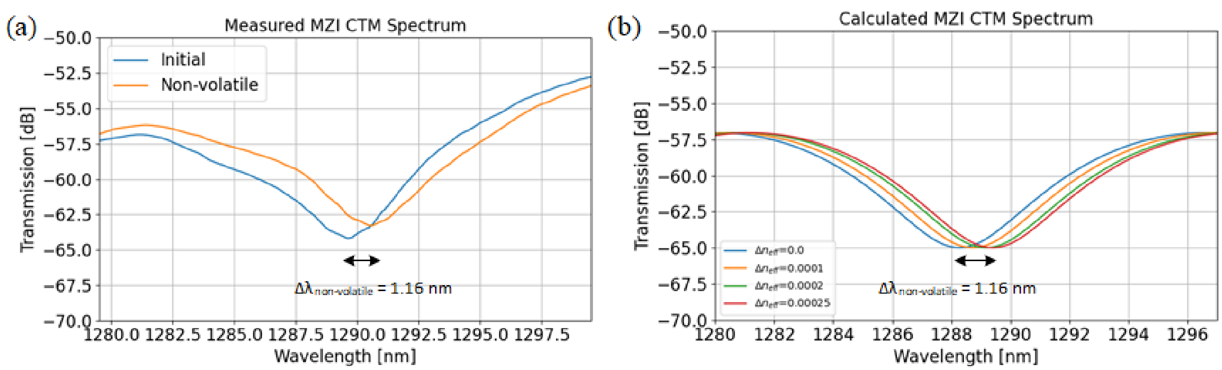

Fig. 9 III-V/Si CTM MZI: (a) measured, and (b) calculated. Measured $\Delta\lambda_{non\text{-}volatile} = 1.16$ nm corresponds to a $\Delta n_{eff,\ non\text{-}volatile} = 2.5 \times 10^{-4}$.

*Fig. 10*a shows the measured transmission spectra of the 2nd order cascaded ring resonator filter described in *Fig. 4*b. The filter shape is far from ideal and modeling indicates power coupling coefficients of $\kappa_0 = 0.43$, $\kappa_1 = 0.02$ for "Ring bank 1" and $\kappa_0 = 0.43$, $\kappa_1 = 0.09$ for "Ring bank 2" as shown in Fig. *10*b. By applying a write operation (0 → + 9 → 0 V), a $\Delta\lambda_{non\text{-}volatile} = 0.041$ is achieved which corresponds to a $\Delta n_{eff,\ non\text{-}volatile} = 1.5 \times 10^{-4}$. This change in effective index is similar to the MZI CTM result ($\Delta n_{eff,\ non\text{-}volatile} = 2.5 \times 10^{-4}$).

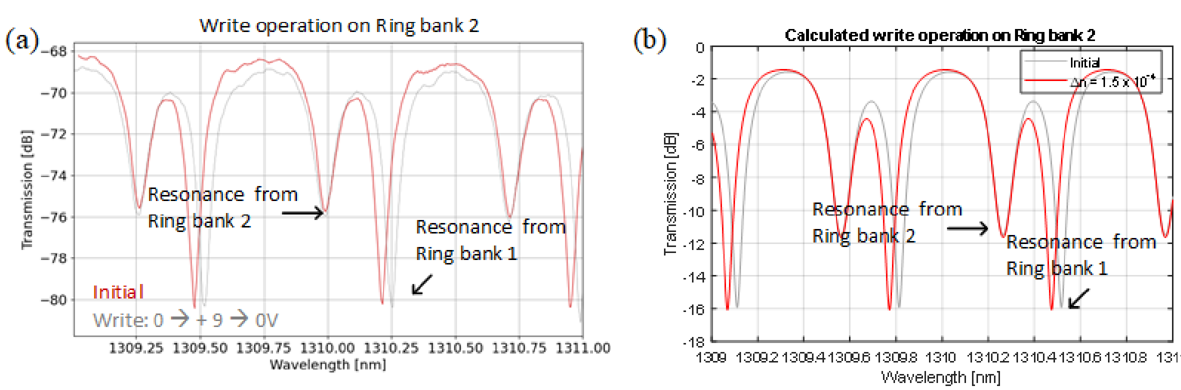

Fig. 10 III-V/Si CTM 2nd order cascaded ring resonator filters: (a) measured, and (b) calculated. Measured $\Delta\lambda_{non\text{-}volatile} = 0.041$ nm corresponds to a $\Delta n_{eff,\ non\text{-}volatile} = 1.5 \times 10^{-4}$.

Non-volatile optical retention measurements for the "write" and "reset" states were performed over a 24 hour period and are shown in Fig. *11*a, and b respectively.

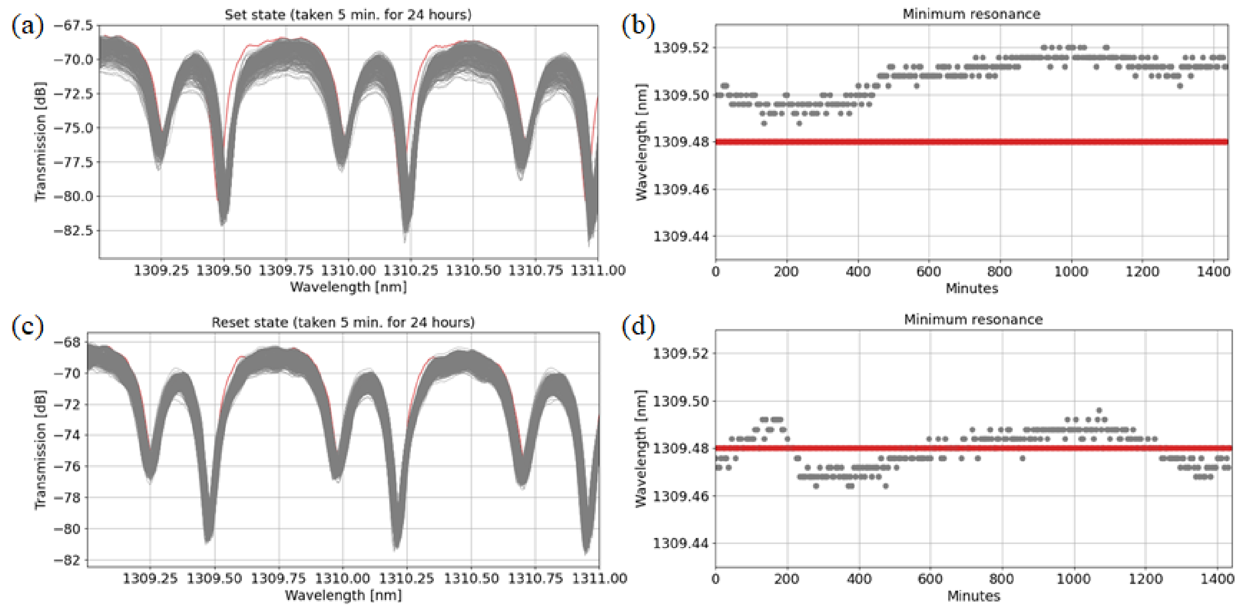

Fig. 11 24 hour data tracking for (a) "write" state optical spectra, (b) non-volatile wavelength shift for a resonant minimum. (c) "Reset" state optical spectra, and (d) non-volatile wavelength reset.

Supplementary Note 4: Transmission electron microscope (TEM) measurements of initial, set, and reset states.

We performed transmission electron microscope (TEM) imaging of initial, set, and reset states as shown in *Fig. 12*a-b respectively. Each image is a separate sample that was biased and subsequently imaged. There does not appear to be any visual evidence of dielectric breakdown in the n-GaAs/Al_2O_3/HfO_2/Al_2O_3/HfO_2/Al_2O_3/Si CTM structure. There are contrast differences and may indicate variability in sample preparation as well as imaging settings. The electron dispersive spectroscopy (EDS) line scans below the TEM images also indicate minimal atomic/interfacial changes.

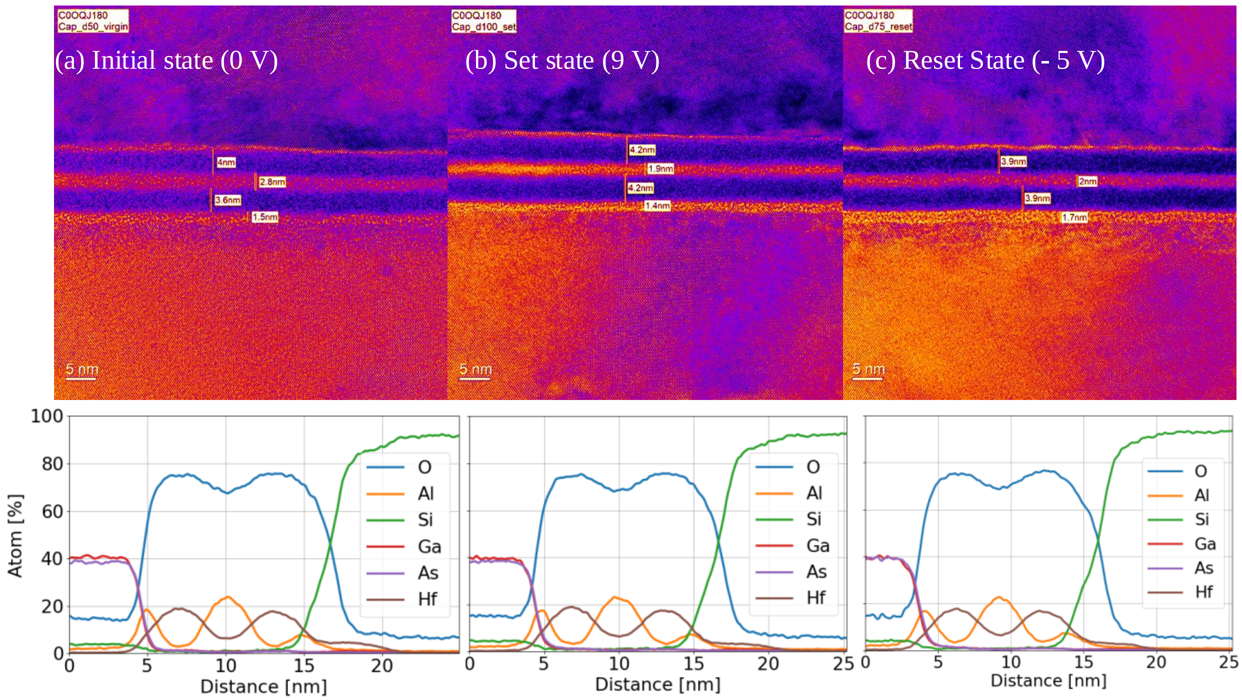

Fig. 12 TEM imaging and EDS line scan of n-GaAs/Al_2O_3/HfO_2/Al_2O_3/HfO_2/ Al_2O_3/Si CTM structure in (a) initial state (0 V), (b) set state (9 V), and (c) reset state (- 5 V).

References

1. Ohno, S. *et al.* Taper-Less III-V/Si Hybrid MOS Optical Phase Shifter using Ultrathin InP Membrane. in *2020 Optical Fiber Communications Conference and Exhibition (OFC)* 1–3 (2020).
2. Ohno, S. *et al.* Taperless Si hybrid optical phase shifter based on a metal-oxide-semiconductor capacitor using an ultrathin InP membrane. 11.

3. Takenaka, M. *et al.* III–V/Si Hybrid MOS Optical Phase Shifter for Si Photonic Integrated Circuits. *J. Lightwave Technol.* **37**, 1474–1483 (2019).

4. Cheung, S. *et al.* Ultra-Power Efficient Heterogeneous III-V/Si De-Interleavers for DWDM Optical Links. in 1–2 (2021). doi:10.1109/GFP51802.2021.9673963.

5. Hiraki, T. *et al.* Heterogeneously integrated III–V/Si MOS capacitor Mach–Zehnder modulator. *Nature Photon* **11**, 482–485 (2017).

6. Hiraki, T. *et al.* Ultrahigh efficiency III-V on Si MOS capacitor optical modulator. in *Silicon Photonics: From Fundamental Research to Manufacturing* (eds. Baets, R. G., O'Brien, P. & Vivien, L.) 19 (SPIE, 2018). doi:10.1117/12.2312315.

7. Atlas User Manual. (2022).

8. Barrios, C. A. & Lipson, M. Silicon Photonic Read-Only Memory. *JOURNAL OF LIGHTWAVE TECHNOLOGY* **24**, 8 (2006).

9. Olivares, I., Parra, J. & Sanchis, P. Non-Volatile Photonic Memory Based on a SAHAS Configuration. *IEEE Photonics Journal* **13**, 9 (2021).

10. Bersch, E., Rangan, S., Bartynski, R. A., Garfunkel, E. & Vescovo, E. Band offsets of ultrathin high-κ oxide films with Si. *Phys. Rev. B* **78**, 085114 (2008).

11. Robertson, J. & Falabretti, B. Band offsets of high K gate oxides on III-V semiconductors. *J. Appl. Phys.* (2014).

12. Feng, Q., Yan, F., Luo, W. & Wang, K. Charge Trap Memory Based on Few-Layered Black Phosphorus.

13. Zhang, Q. *et al.* Band offset and electron affinity of MBE-grown SnSe2. *Appl. Phys. Lett.* (2018).

14. Spassov, D. *et al.* Charge Storage and Reliability Characteristics of Nonvolatile Memory Capacitors with HfO2/Al2O3-Based Charge Trapping Layers. 15 (2022).

15. Xiong, H. D. *et al.* Characterization of electrically active defects in high-k gate dielectrics by using low frequency noise and charge pumping measurements. *Microelectronic Engineering* (2007).

16. She, M. Semiconductor Flash Memory Scaling. 133.

17. You, H.-C. *et al.* SONOS-Type Flash Memory Using an HfO2 as a Charge Trapping Layer Deposited by the Sol–Gel Spin-Coating Method. 3.

18. Zhang, Y. *et al.* Defect states and charge trapping characteristics of HfO2 films for high performance nonvolatile memory applications. *Appl. Phys. Lett.* 6 (2014).

19. Cerbu, F. Intrinsic electron traps in atomic-layer deposited HfO2 insulators. *Appl. Phys. Lett.* (2016).

20. Palik, E. *Handbook of Optical Constants of Solids*. vols 1–5.

21. Chrostowski, L. & Hochberg, M. *Silicon Photonics Design: From Devices to Systems*. (Cambridge: Cambridge University Press, 2015).

22. Reed, T., Mashanovich, G., Gardes, Y. & Thomson, J. Silicon optical modulators. *nature photonics* **4**, (2010).

23. Bogaerts, W. *et al.* Silicon microring resonators. *Laser Photonics Rev.* 27 (2011).

24. Ohno, S., Toprasertpong, K., Takagi, S. & Takenaka, M. Si microring resonator crossbar array for on-chip inference and training of optical neural network. 38.

25. Heyn, P. D. Receivers Based on Silicon Ring Resonators for Multi-Wavelength Optical Interconnects. 270.

26. De Heyn, P. *et al.* Fabrication-Tolerant Four-Channel Wavelength-Division-Multiplexing Filter Based on Collectively Tuned Si Microrings. *J. Lightwave Technol.* **31**, 2785–2792 (2013).

27. Bogaerts, W. & Selvaraja, S. K. Compact Single-Mode Silicon Hybrid Rib/Strip Waveguide With Adiabatic Bends. *IEEE Photonics J.* **3**, 422–432 (2011).